

Characteristics of aeolian deposits and evolution of surface process since 15.5 ka in the Zoige Basin, northeastern Tibetan Plateau

Dou Chen ^a, Jiangli Pang ^{a,*}, Xiaochun Zha ^a, Chunchang Huang ^a, Yuzhu Zhang ^b, Yali Zhou ^a, Yuqin Li ^a, Meihui Zhang ^a, Ruiqi Huang ^a, Xinran Fan ^a

^a School of Geography and Tourism, Shaanxi Normal University, Xi'an 710119, China

^b Shaanxi Key Laboratory of Earth Surface System and Environmental Carrying Capacity, College of Urban and Environmental Sciences, Northwest University, Xi'an 710127, China

ARTICLE INFO

Editor: Dr. Pradeep Srivastava

Keywords:

Aeolian deposits
Surface process
Late Pleistocene
Paleo-lakeshore terraces
Northeastern Tibetan Plateau

ABSTRACT

Aeolian deposits in the Zoige Basin provide direct evidence for understanding the evolution of the surface environment after the disappearance of the paleolake. The complete aeolian sequence was deposited on the paleo-lakeshore terraces of the Tangke ancient city area. This study focuses on the TKGC section, a representative aeolian deposit on the paleo-lakeshore terrace, and conducts a systematic investigation of its sedimentological, micromorphological, geochemical, and chronological characteristics. The results show that: (1) The chronostratigraphic framework of the TKGC section is as follows: aeolian sand (15.5–13.6 ka BP)—aeolian loess (13.6–8.5 ka BP)—paleosol (8.5–3.0 ka BP)—recent loess (3.0–1.3 ka BP)—topsoil (1.3–0 ka BP). (2) Consistent with previous understandings of global climate change, the loess and paleosol sequences in the alpine Zoige basin also reflect varying intensities of weathering and pedogenesis during different periods. Sedimentological, geochemical, and micromorphological evidence consistently indicate strong pedogenesis during the paleosol development, while pedogenic processes were weak during periods of aeolian sand and loess accumulation. (3) Following the disappearance of the paleolake, from 15.5 to 13.6 ka BP, the region experienced harsh climatic conditions and intense aeolian activity, leading to the deposition of coarse-grained aeolian sand. Around 13.6 ka BP, aeolian activity declined, resulting in the accumulation of finer-grained aeolian loess. By 8.5 ka BP, the regional climate shifted from cold and arid to warm and humid, initiating the development of the paleosol. Around 3.0 ka BP, climatic conditions reverted to colder and drier states, enhancing aeolian processes and facilitating the formation of the recent loess layer. Subsequently, around 1.3 ka BP, the topsoil began to form atop the recent loess deposits.

1. Introduction

The northeastern (NE) Tibetan Plateau is not only the source region of the Yellow River but also a critical area for water resources and ecological conservation in China (Li et al., 2020). This region contains extensive lakes, glaciers, wetlands, and grasslands, forming a unique hydrological and ecological system that is highly sensitive to global climate change and human activities (Chen et al., 2020; Dong et al., 2010; Yang et al., 2021). The Zoige Basin, a faulted depression formed during the Quaternary uplift of the Tibetan Plateau, is the largest alpine wetland in China. Often referred to as the “reservoir” of the Yellow River, its wetlands contribute nearly 30 % of the river's total discharge (Hu et al., 2023; Jia et al., 2022a; Zhao et al., 2024). In recent years, the

NE Tibetan Plateau has experienced significant environmental challenges, including glacial retreat, grassland degradation, and desertification (Hu et al., 2015; Li et al., 2019; Zhi et al., 2024). The rapid shrinkage of wetlands in the Zoige Basin has already endangered local terrestrial and aquatic ecosystems, as well as water supply to the upper reaches of the Yellow River (Dong et al., 2020; Hu et al., 2017; You et al., 2014; Yang et al., 2024). At the same time, grassland degradation has accelerated land desertification, posing severe threats to both the environment and local communities. Therefore, investigating the potential links between surface processes and climate change is essential for understanding both current and future environmental dynamics in the Zoige Basin and the broader NE Tibetan Plateau.

Extensive research has demonstrated that the Zoige Basin sustained a

* Corresponding author.

E-mail address: jlpang@snnu.edu.cn (J. Pang).

lacustrine environment for a prolonged period during the Quaternary. The gradual disappearance of the paleolake was triggered by fluvial capture and diversion of its outflow by the Yellow River. This hydrological reorganization led to profound transformations in the region's surface environment (Huang, 2021; Wang et al., 2023; Zhu et al., 2025). However, the timing of the initial disappearance of the paleolake remains a subject of debate. As the lakebed became exposed, new surface processes emerged, resulting in the development of diverse sedimentary deposits. These deposits offer direct evidence for reconstructing environmental changes, with aeolian sediments specifically reflecting the dynamics and fluctuations of regional aeolian dust activity.

Despite these favorable conditions, research on aeolian deposits remains limited. Existing studies have primarily focused on short-term aeolian activity and its impacts on pastoralism (Han et al., 2023; Wang et al., 2024b; Bai et al., 2013), while long-term records are lacking, leaving many key issues unresolved. Disagreements persist regarding the onset and evolution of aeolian dust activity and their relationship with climate change. Hu et al. (2018) suggest that dust activity began in the early Holocene, while Zhou et al. (2022) argue for an even earlier origin during the late Pleistocene, although its development and evolution have not been systematically studied. Jia et al. (2022b) report strong dust activity during the early and late Holocene, with a weaker phase in the mid-Holocene. In contrast, Hu et al. (2017) claim that aeolian dust activity was primarily concentrated in the late Holocene, with minimal activity during the early to middle Holocene. The results of Zhao et al. (2024) indicate that the earliest aeolian activity occurred around 10 ka BP. These discrepancies and research gaps are mainly attributable to the complex geomorphology of the Zoige Basin, the unclear environmental significance of climate proxies in alpine regions, the scarcity of reliable chronological data, and the limited availability of long-term aeolian sequences, all of which limit the accurate identification and reconstruction of aeolian sand activity and its evolution. Clearly, the identification of a well-preserved, long-term sequence of aeolian deposits is crucial for extracting robust paleoenvironmental signals and addressing these challenges.

The accumulation and preservation of aeolian deposits require specific geomorphic conditions. Although the former lakebed of the Zoige Basin is relatively flat, its current dominance by wetlands and grassland makes it unfavorable for the effective preservation of aeolian deposits. The surrounding area, characterized by low hills and steep slopes, also poses challenges for sediment preservation. However, flat geomorphic surfaces—such as paleo-lakeshore terraces, river terraces, and the margins of flashflood fans—can provide favorable conditions for the preservation of aeolian sequences. This study focuses on the Tangke ancient city (TKGC) section, a typical aeolian deposit located on the paleo-lakeshore terrace. Through integrated analyses of sedimentology, micromorphology, geochemistry, and chronology, this study aims to (1) identify the earliest possible time of aeolian activity after the disappearance of the Zoige paleolake; (2) examine the characteristics and timing of changes in aeolian sand activity intensity; and (3) reconstruct surface process evolution in the Zoige Basin since the late Pleistocene. The findings provide essential data for understanding regional environmental changes after the disappearance of the Zoige Paleolake.

2. Geographical setting and sampling

The Zoige Basin is located in the NE Tibetan Plateau, bordered by the Anyemaqen Mountains to the west, the Min Mountains to the east, the Xiqing Mountains to the north, and the Qionglai Mountains to the south. Covering an area of approximately 19,600 km², the basin is a faulted depression formed during the uplift of the Tibetan Plateau. The paleolakebed forms a broad, flat plain, while paleo-lakeshore terraces are distributed along the foothills of bedrock hills both within and surrounding the basin. The Yellow River has developed one to two levels of terraces in the region, with relatively flat surfaces. Extensive outwash/flashflood deposits are distributed around the basin margins. Composed

mainly of gravel, these fan surfaces gently slope toward the basin's center. The region experiences alpine-humid climate characterized by only two distinct seasons: a long, cold winter and a short, mild summer. Daily temperature variation is large. The annual mean temperature ranges from 1.1 °C to 1.2 °C, with the highest temperatures occurring in July (10.9 to 12.7 °C) and the lowest in January (-8.2 to -10.2 °C) (Jin et al., 2025; Li et al., 2016). Annual precipitation is approximately 600–650 mm, mostly falling between late May and mid-July, while annual evaporation averages 1347 mm. Ground freezing typically begins in late September and thaws completely by mid-May (Li et al., 2014). The region receives an average of 2400 h of sunshine per year (Pang et al., 2024). The core region of the basin, along with the surrounding low, gentle areas, is primarily covered by subalpine meadows. The dominant plant species in these communities are sedges, particularly Schoenus species, with associated plants including Artemisia, Poaceae, and Ranunculaceae. In the lower-lying areas of the basin, marsh meadows and swamp vegetation are prevalent. In higher-altitude hill regions, sparse shrublands and alpine evergreen coniferous forests are found. The primary soil types are subalpine and swamp meadow soil (Wang et al., 2021) (Fig. 1).

Studied sites: CLQ, XQN and TWR section (Wang, 2023); OQC section (Zhao et al., 2024).

Unstudied sites: XMMC (Xiaman Ranch); XC (Xicang Village); LH (Luohua Village); SZ (Suozang Village).

Along the right bank of the Baihe River, between Tangke Town and the Baihe River estuary, a flat terrace is clearly visible approximately 10–15 m above the river channel, situated 500–1000 m from the river. This terrace has a gentle slope toward the river and gradually transitions into low bedrock hills at rear edge. It stretches more than 5 km in north-south direction and exceeds 300 m in width (Fig. 1c). Field investigations indicate that no well-developed fluvial terraces are present in this section of the Baihe River. Although this landform is comparable in height to the first-level fluvial terrace, its surface is exceptionally flat and lacks fluvial deposits, suggesting that it represents the former lakebed of the Zoige paleolake rather than a fluvial terrace.

Based on their elevation, the terraces adjacent to the paleo-lakebed represent the paleo-shoreline zones of the Zoige paleolake. Comparable paleo-lakeshore terraces have also been identified at nearby locations such as XMMC, XC, LH, and SZ sections. Following the retreat of the paleolake, these terraces were exposed as terrestrial surfaces. Among them, areas with relatively gentle slopes provided favorable geomorphic conditions for the accumulation and preservation of aeolian deposits.

Field investigations revealed that the aeolian deposits clearly overlie a thick layer of lacustrine deposits. These lacustrine sands typically exhibit a gray-green color, silty to sandy texture, granular structure, high porosity, and remarkable uniformity in color, structure, and composition. Their thickness exceeds 5 m, with no bottom exposed, and they extend laterally in a stable manner. Further investigation showed that this thick gray-green sand layer lies directly atop the bedrock and is spatially consistent across the area. These findings indicate that the gray-green sands represent littoral facies deposits of the Zoige paleolake, resting directly on bedrock.

The TKGC section was selected for detailed analysis. It is located near the Tangke ancient city ruins (33°27'8.58"N, 102°29'6.93"E) at an elevation of 3449 m. The section is exposed along a naturally formed escarpment, with well-preserved, undisturbed stratigraphy that is clearly defined and continuous (Fig. 1c). From top to bottom, the stratigraphy is divided into the following units: topsoil (TS)—recent loess (L₀)—paleosol (S₀)—aeolian loess (L₁)—aeolian sand (AS)—lacustrine sand (LS), with the lacustrine layer directly overlying bedrock. Detailed stratigraphic descriptions are provided in Table 1.

3. Methods

Following the cleaning of the section in the field, bulk rock samples were systematically collected at 2 cm intervals from the top down to a

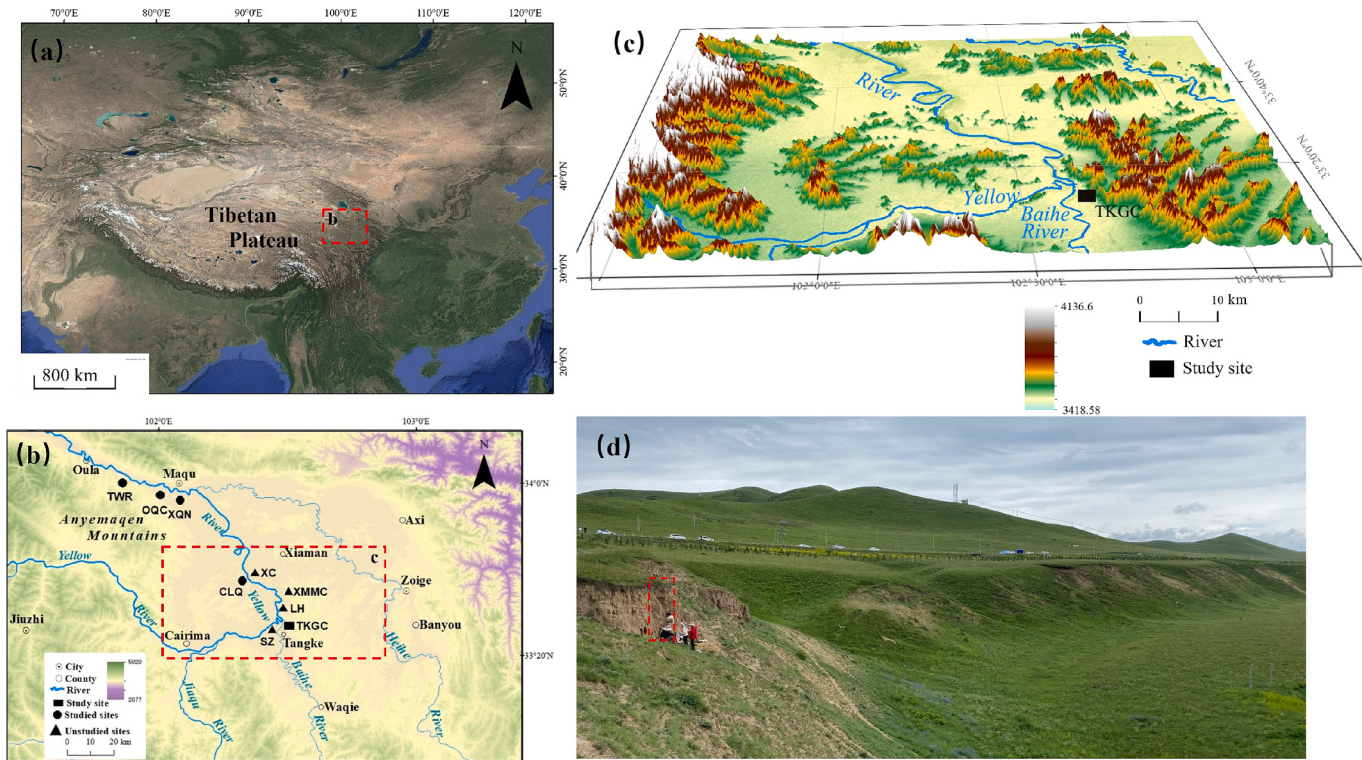


Fig. 1. (a) Map showing the Zoige Basin (red square) on the NE Tibetan Plateau; (b) Overview map of the Zoige Basin region; (c) Geomorphic characteristics of the eastern area of the Zoige paleolake; (d) Geomorphic characteristics of the TKGC section. (For interpretation of the references to color in this figure legend, the reader is referred to the web version of this article.)

Table 1
Pedostratigraphic divisions and descriptions of the TKGC section on the paleolakeshore terraces of the Zoige Basin.

Depth (cm)	Pedostratigraphy	Pedosedimentary descriptions
0–50	Topsoil (TS)	Gray yellow brown (10YR 4/2), fine sandy-silt with a granular structure, loose and porous, containing a dense network of plant roots intertwined with both coarse and fine roots, presenting a typical felt structure.
50–104	Recent loess (L ₀)	Muddy yellow orange (10YR 6/3), fine sandy-silt texture, homogeneous massive structure, relatively loose, with numerous small voids filled with slender roots and containing a small amount of calcareous pseudomycelium.
104–244	Paleosol (S ₀)	Gray brown (7.5YR 4/2), silt texture, granular-blocky structure, containing various-sized voids and vertical fissures, with abundant calcareous pseudomycelium on the structural surfaces.
244–324	Aeolian loess (L ₁)	Muddy yellow orange (10YR 7/3), fine sandy-silt texture, homogeneous massive structure, relatively loose, with numerous small voids. Calcareous pseudomycelium are present on structural surfaces but are significantly fewer than in the S ₀ .
324–354	Aeolian sand (AS)	Muddy yellow orange (10YR 6/4), silt-fine sand texture, blocky structure, relatively loose. Typical lacustrine sand, thickly bedded (>300 cm). Gray green (5YR 5/2), fine sand-sand texture, granular structure, and uniformly loose. With regular thin horizontal bedding. The color, texture, and structure are highly uniform, and the unit exhibits well-developed horizontal bedding, directly overlying the bedrock.
354?	Lacustrine sand (LS)	

depth of 370 cm, resulting in a total of 185 samples. Additionally, 22 undisturbed block samples were obtained for micromorphological analysis to ensure the integrity and representativeness of their original structures. At key stratigraphic horizons, seven chronological samples were taken, with their locations provided in **Table 2**. The chronological samples are collected by inserting a black plastic bag into one end of the stainless-steel tube contact section, driving the other end into the fresh section using a hammer, filling the inner end with the same material upon tube removal, and finally sealing it with tinfoil and tape.

Optically stimulated luminescence (OSL) dating was carried out on a Risø-TL/OSL-DA20 Dating System using the single aliquot regenerative-dose (SAR) protocol (Murray and Wintle, 2000). In a darkroom, 2–3 cm was removed from both ends of each steel tube for measuring water content and concentrations of U, Th, Rb and K. The remaining, unexposed sediment was treated with 10 % HCl and 30 % H₂O₂, and the 90–125 µm grain-size fraction was extracted. This fraction was subsequently etched with 40 % HF to remove the α-irradiated outer layers of both feldspar and quartz grains. Finally, the samples were oven-dried for further analysis. The U, Th, Rb, and K concentrations were carried out in the China Geological Survey Xi'an Geological Survey Center. The water content of the OSL samples was determined by the change in water content before and after air-drying of the laboratory samples. Considering the changes in soil water content in geological history, 3 % uncertainty was added. The cosmic ray-dose rate was derived from parameters such as latitude, longitude, elevation, and burial depth of the location where the sample was taken, combined with relevant formulas (Prescott and Hutton, 1994). Finally, the total dose rates were estimated based on the relevant equations proposed by Adamiec and Aitken (1998).

Grain-size analysis was performed as follows: After air-drying, 1 g of soil sample (weighed to an accuracy of 0.0001 g) was placed in a beaker and labeled. Organic matter and calcareous cement were sequentially removed by treating the samples with 10 % H₂O₂ and 10 % HCl. After the reactions were complete, the samples were rinsed with deionized water

Table 2

OSL dating results of the TKGC section on the paleo-lakeshore terraces of the Zoige Basin.

Sample ID	Sediment and stratigraphy	Depth (cm)	Th ($\mu\text{g/g}$)	U ($\mu\text{g/g}$)	Rb ($\mu\text{g/g}$)	K (%)	Water content (%)	Equivalent dose (Gy)	OSL age (ka)
OSL-1	Recent loess	70–75	10.48 ± 0.7	1.71 ± 0.3	105.81 ± 5	1.77 ± 0.04	25 ± 3	4.78 ± 0.18	1.80 ± 0.09
OSL-2	Recent loess	90–95	10.37 ± 0.7	2.58 ± 0.4	118.83 ± 5	1.85 ± 0.04	22 ± 3	6.43 ± 0.24	2.16 ± 0.11
OSL-3	Paleosol	115–120	8.02 ± 0.6	1.34 ± 0.3	84.5 ± 4	1.86 ± 0.04	23 ± 3	9.17 ± 0.13	3.61 ± 0.12
OSL-4	Paleosol	160–165	11.45 ± 0.7	2.5 ± 0.3	118.68 ± 5	1.91 ± 0.04	23 ± 3	13.31 ± 0.18	4.48 ± 0.14
OSL-5	Paleosol	230–235	11.38 ± 0.7	2.05 ± 0.3	119.86 ± 5	1.89 ± 0.04	21 ± 3	24.02 ± 0.36	8.31 ± 0.28
OSL-6	Aeolian loess	295–300	10.98 ± 0.7	2.58 ± 0.4	122.29 ± 5	1.95 ± 0.04	20 ± 3	38.06 ± 0.65	12.61 ± 0.45
OSL-7	Aeolian sand	340–345	13.05 ± 0.8	1.88 ± 0.3	145.09 ± 6	2.18 ± 0.04	20 ± 3	47.68 ± 0.73	15.00 ± 0.49

and allowed to settle for 72 h. An appropriate amount of $(\text{NaPO}_3)_6$ was then added to ensure complete particle dispersion, followed by 5 min of ultrasonic agitation prior to measurement. Grain-size was analyzed using an LS13320 laser analyzer with a precision of 1 %.

For geochemical element analysis, air-dried samples were ground to pass through a 200-mesh sieve, after which 4 g of the powder was pressed into pellets using a YYJ40 hydraulic press. Geochemical elements were determined using Bruker S2 RANGER Energy Dispersive X-ray fluorescence spectrometer. During the experiment, a standard soil

reference sample (BAXS178 S2) is added for calibration, with the error controlled within 5 %. Geochemical indicators used in this study include the chemical index of alteration (CIA), calculated as $\text{Al}_2\text{O}_3/(\text{Al}_2\text{O}_3 + \text{K}_2\text{O} + \text{Na}_2\text{O} + \text{CaO}^*)$, and the weathering-leaching index (ba), calculated as $(\text{K}_2\text{O} + \text{CaO}^* + \text{Na}_2\text{O} + \text{MgO})/\text{Al}_2\text{O}_3$. In these formulas, all oxide values are expressed in molar fractions, and CaO^* represents the calcium oxide content derived exclusively from silicate minerals. Since CaO and Na_2O usually occur in approximately equal proportions in silicates, when $m(\text{CaO})$ is greater than $m(\text{Na}_2\text{O})$, $m(\text{CaO}^*)$ is taken as equal to $m(\text{Na}_2\text{O})$;

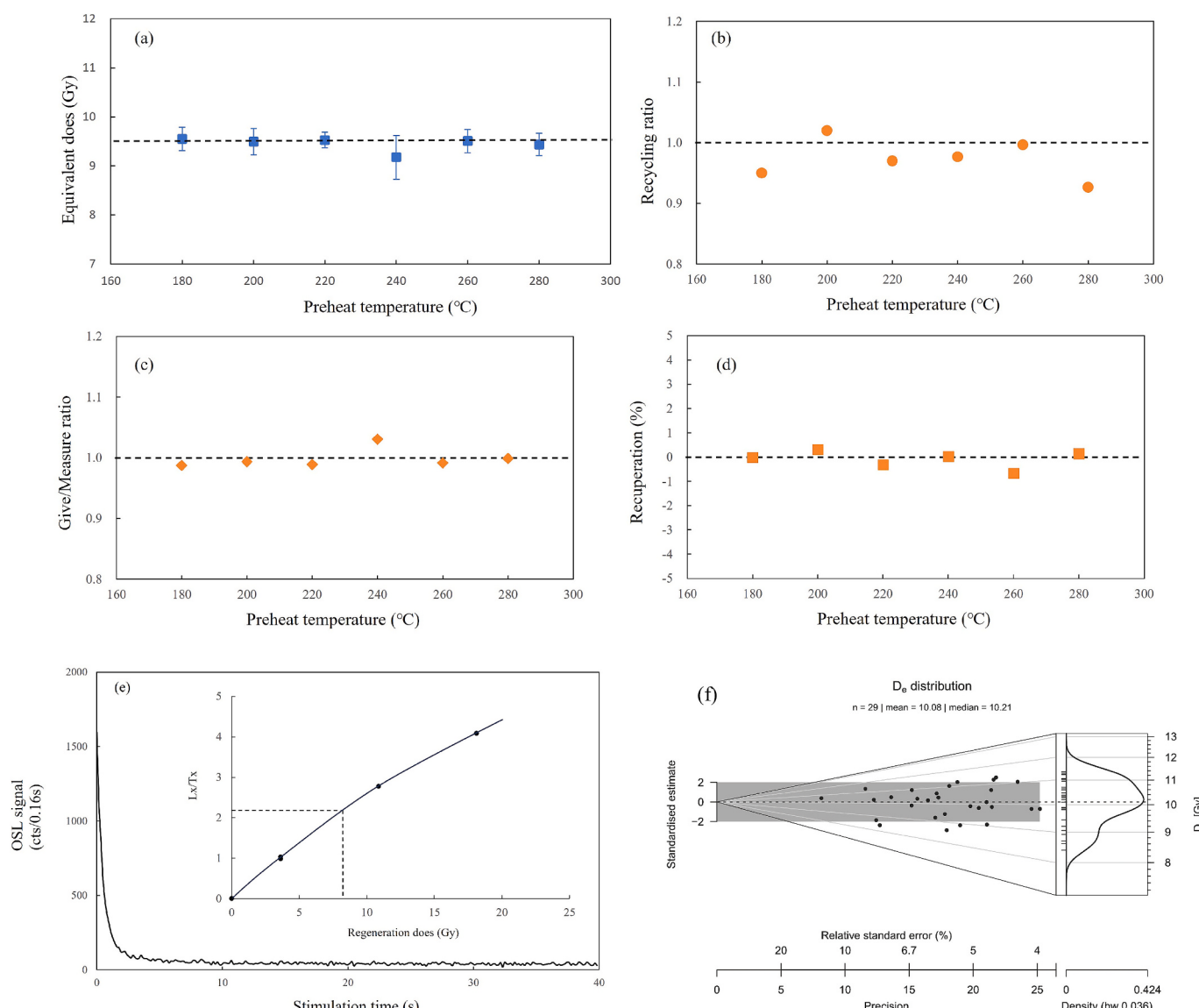


Fig. 2. (a-d)Preheat plateau test results using the sample OSL-3; (e) Decay curves and growth curve of the sample OSL-3; (f) The radial plots of the De values for sample OSL-3.

conversely, when $m(\text{CaO})$ is less than or equal to $m(\text{Na}_2\text{O})$, $m(\text{CaO}^*)$ is taken as equal to $m(\text{CaO})$. The Rb/Sr ratio was calculated based on elemental concentrations. Magnetic susceptibility was analyzed by a Bartington MS-2B magnetic susceptibility meter (0.47/4.7 kHz).

The intact block samples were impregnated with epoxy resin and cured, then cut into 35 mm × 25 mm × 20 mm pieces for thin section preparation using a DPM-250 A/300 A grinding machine. Soil micromorphological units were observed, analyzed, and described under a Leica DMRX polarizing microscope at magnifications of 2.5 × 10 to 50 × 10. Descriptions focused on mineral characteristics (type, formation time, morphology, size, occurrence state, and distribution), organic matter distribution (type, quantity, and distribution), and void (type, size, quantity, and distribution). The terminology for micromorphology follows the reference (Stoops, 2003).

4. Results

4.1. OSL Dating results

Establishing appropriate measurement conditions is critical for obtaining reliable equivalent dose (D_e) values. In this study, sample OSL-3 was selected for conducting preheat temperature plateau tests. Preheat temperatures ranged from 180 °C to 280 °C in 20 °C intervals, each held for 10 s. The results showed a clear plateau in the 180–220 °C range. Within this temperature interval, the give/measure ratios ranged from 0.98 to 1.09, the recycling ratios ranged from 0.91 to 1.08, and the recuperation is less than 5 % (Fig. 2a-d). Based on these results, a preheat temperature of 220 °C and a cutheat of 180 °C were selected as the measurement conditions for D_e determination. The sample OSL-3 exhibited rapid decay of luminescence intensity to background levels, indicating a strong dominance of fast components in the decay curve. This suggests that the sample was well-bleached before burial. The quartz growth curve derived from experimental data passes through the origin and does not reach saturation (Fig. 2e), and the D_e values of OSL-3 are narrowly distributed, following a normal distribution with low overdispersion ($OD = 5.93\%$) (Fig. 2f). These characteristics indicate thorough exposure to sunlight before deposition. The detailed OSL dating results are presented in Table 2.

4.2. Grain-size characteristics

4.2.1. Grain-size natural frequency distribution

In the TKGC section, the lacustrine sand (LS) below 354 cm exhibits grain-size natural frequency distribution distinctly curve different from that of the overlying aeolian deposits above 354 cm. The distribution

curve of the LS shows a sharply peaked shape shifted toward coarser grains. The primary peak modal grain-size is 176.9 μm, corresponding to the medium sand fraction, with the highest content of 6.78 %—this represents the largest primary peak grain-size among all sedimentary layers. The secondary peak modal size is 8.14 μm, with the lowest content across all layers. These characteristics indicate that the LS differ significantly in grain-size properties from the aeolian deposits and are consistent with coarser grain-size features typical of lacustrine deposits (Fig. 3).

Above 354 cm, the grain-size natural frequency distribution curves of the aeolian deposits show a bimodal distribution and shift toward finer grains. The primary peak ranges from 52.63 to 82.9 μm, while the secondary peak ranges from 7.42 to 10.78 μm. The grain-size distribution curves vary notably among different stratigraphy. Aeolian sand (AS) and loess (L) layers have primary peaks at 76.43 μm and 69.62 μm, respectively, both within the fine sand range. However, the primary peak content of AS (3.70 %) is higher than that of L (3.07 %), suggesting stronger aeolian sand activity during the deposition of AS compared to L. The paleosol (S_0) shows a primary peak at 52.63 μm in the coarse silt range, with a peak content of 3.94 %, higher than both AS and L. This indicates weaker aeolian sand activity and stronger pedogenesis during the deposition of S_0 .

4.2.2. Grain-size parameter characteristics

The median grain-size (M_d) and mean grain-size (M_z) are used to reflect the average particle size and coarseness of the sediment, and they also indicate the degree of concentration in the grain-size distribution. The standard deviation (δ) indicates the sorting degree of the sediments, that is, the uniformity of particle sizes. In the three-dimensional characteristic distribution plot of grain-size parameters (M_d , M_z , and δ), the aeolian deposit samples are roughly aligned along a single linear trend, while the LS samples are clearly offset from this trend, indicating distinct depositional environments (Fig. 4). The LS samples exhibit relatively high M_d (75.76–112.60 μm) and M_z (85.08–105.53 μm) values, and lower δ values (2.30–2.58), suggesting coarser grain-size with better sorting—features typical of lacustrine deposits.

For the aeolian deposits, the M_d ranges from 29.57 to 97.31 μm, the M_z from 36.15 to 97.94 μm, respectively, the δ from 2.16 to 2.93. Among the aeolian deposits, the AS has the highest M_d (66.93 μm), M_z (79.03 μm), and δ (2.63), indicating the coarsest grain-size and the poorest sorting. This is followed by the aeolian loess L_1 (41.45 μm, 52.33 μm and 2.49) and recent loess L_0 (42.69 μm, 50.53 μm and 2.37). The S_0 has the lowest values (36.48 μm, 42.28 μm and 2.32), indicating the finest grain-size and the best sorting among the aeolian layers.

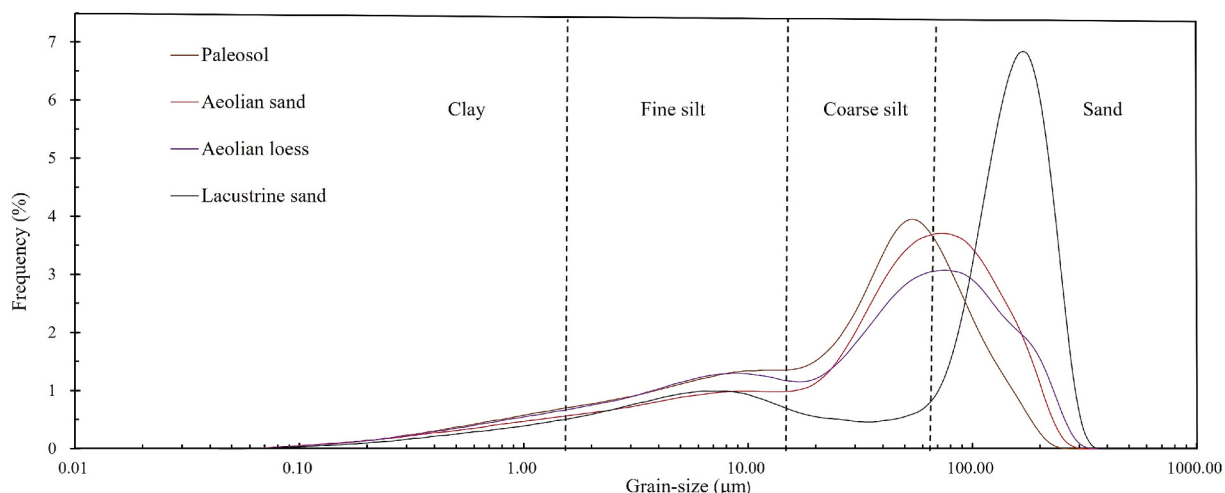


Fig. 3. Grain-size distribution frequency curves of the TKGC section on the paleo-lakeshore terraces of the Zoige Basin.

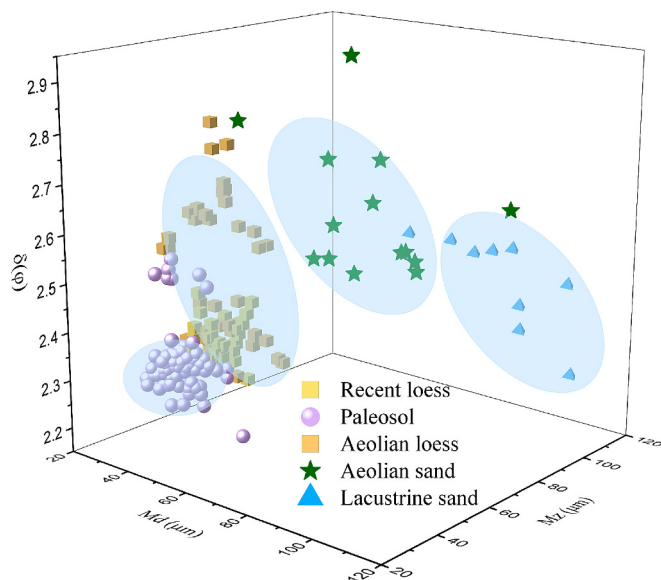


Fig. 4. Three-dimensional characteristics of grain-size of the TKGC section on the paleo-lakeshore terraces of the Zoige Basin.

4.2.3. Grain-size distribution

The LS is dominated by sand-sized grains ($>63 \mu\text{m}$), accounting for 61.36 %, with an average grain-size of 95.44 μm . Other grain-size fractions occupy relatively small proportions. In contrast, the aeolian deposits are primarily composed of silt-sized grains, with an average grain-size of 49.38 μm , and show a significant increase in clay content compared to LS, indicating that LS and the aeolian deposits were formed in distinct sedimentary environments (Fig. 5).

Among the aeolian deposits, different sedimentary layers display clear differences in grain-size distribution. The AS contains the lowest clay content (10.37 %) and fine silt (21.52 %), but the highest sand (52.15 %), reflecting intense aeolian sand activity during its deposition.

In the L₁, clay (11.09 %) and fine silt (22.90 %) contents are higher than in the AS, while sand content (36.29 %) is lower, indicating a finer grain-size and weaker wind activity compared to AS during the deposition period. The S₀ shows even higher values of clay (11.48 %) and fine silt (23.11 %), but the lowest sand content (29.07 %), suggesting further weakened wind activity and stronger pedogenesis during this period. Compared to the S₀, the L₀ exhibits decreased clay and fine silt contents but increased sand content, implying a renewed strengthening of aeolian sand activity during this interval. The clay/sand ratio curve also reflects variations in wind strength across different stratigraphy: It reaches a maximum in the S₀ (0.4), decreases in the L₁ and L₀ (both 0.31), and is the lowest in the AS (0.20), further indicating differential wind intensities during their respective depositional period.

4.3. Element contents

4.3.1. Major Element contents and geochemical parameters

In the TKGC section, SiO₂, Al₂O₃, and Fe₂O₃ constitute the major components, followed by K₂O, Na₂O, CaO, and MgO. Their concentrations decrease in the order of SiO₂ (670.4 g/kg) > Al₂O₃ (126.6 g/kg) > Fe₂O₃ (37.4 g/kg) > K₂O (22.4 g/kg) > Na₂O (18.7 g/kg) > CaO (15.9 g/kg) > MgO (13.6 g/kg). Na₂O and CaO contents reach minimum values in the paleosol (S₀) (17.8 g/kg and 14.8 g/kg, respectively), indicating intense weathering and pedogenesis that facilitated the leaching of soluble elements. In contrast, the highest concentrations of Na₂O and CaO occur in the aeolian sand (AS) (20.1 g/kg and 23.1 g/kg), reflecting relatively weak weathering during this period. High Na₂O and CaO values are also observed in the aeolian loess (L₁) and recent loess (L₀), but these are lower than in AS. The contents of Al₂O₃, MgO, and K₂O show similar distribution patterns that are inversely related to those of Na₂O and CaO. These elements peak in the S₀ (130.30 g/kg, 15.78 g/kg, and 23.54 g/kg, respectively) and exhibit lower values in the L and AS (Table 3).

Different geochemical parameters reflect chemical weathering characteristics from various perspectives. The CIA indicates the degree of feldspar weathering into clay minerals (Chen et al., 2022; Nesbitt and

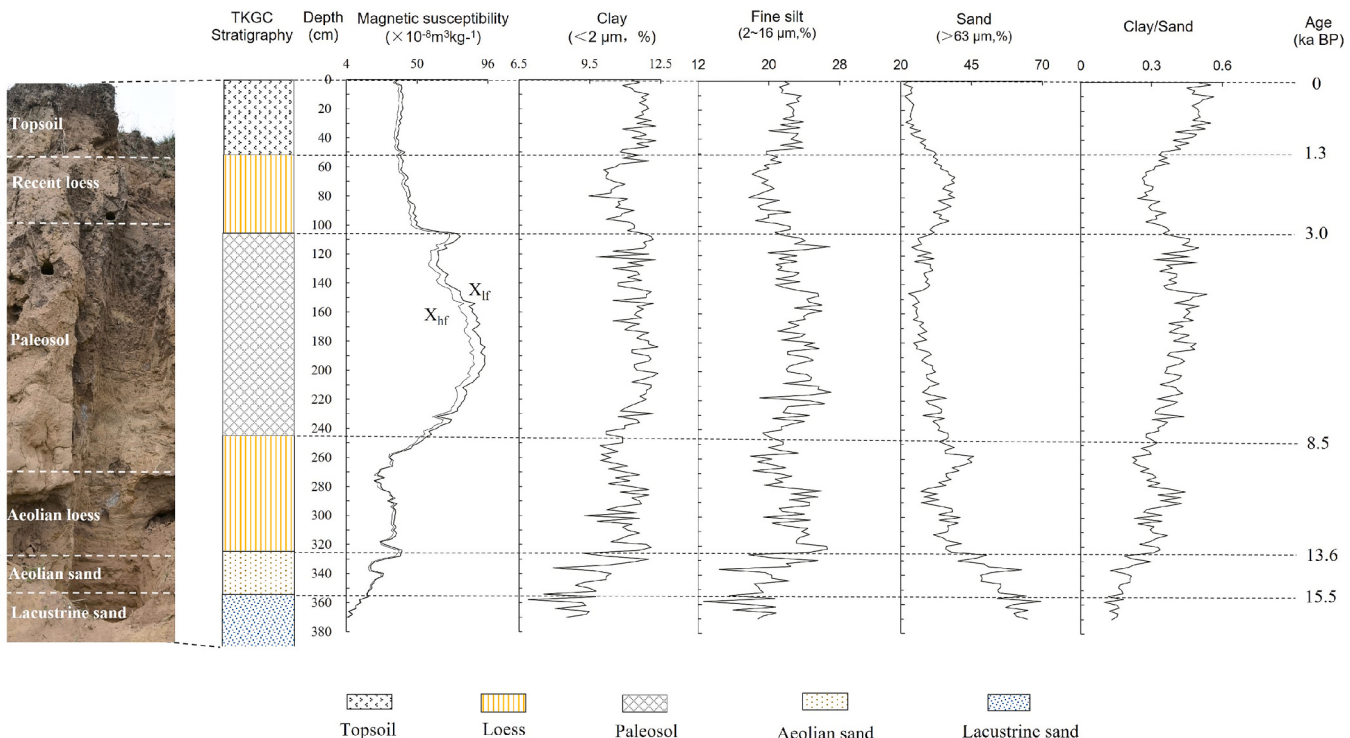


Fig. 5. Magnetic susceptibility and grain-size content curves of the TKGC section on the paleo-lakeshore terraces of the Zoige Basin.

Table 3

The major element contents of the TKGC section on the paleo-lakeshore terraces of the Zoige Basin.

Pedostratigraphy	Depth (cm)	SiO ₂ (g/kg)	Al ₂ O ₃ (g/kg)	MgO (g/kg)	K ₂ O (g/kg)	Na ₂ O (g/kg)	CaO (g/kg)
Recent loess	50–104	678.4	122.7	13.1	21.1	19.1	15.1
Paleosol	104–244	670.8	130.30	15.78	23.54	17.8	14.8
Aeolian loess	244–324	650.7	128.7	15.3	23	18.2	17.9
Aeolian sand	324–354	668.1	132.5	13.5	24.5	20.1	23.1

Young, 1984, 1989). The CIA value in the S₀ (61.19) is higher than those in the L₁ (57.60) and L₀ (58.50), suggesting higher degree of feldspar alteration and stronger weathering during the development of S₀ (Fig. 6). The ba index reflects the leaching and migration intensity of soluble elements such as Ca and Na during pedogenesis, decreases with increasing leaching intensity. In the TKGC section, the ba value is lowest in the S₀ (0.55) and higher in the L₁ and L₀ (0.62 and 0.59, respectively), indicating stronger leaching during the deposition of the S₀. Because Rb has larger ionic radius and is easily adsorbed by clay minerals, whereas Sr has smaller radius and is more likely to be leached during the weathering of detrital carbonates (Wang et al., 2024a; Zhai et al., 2025), the Rb/Sr ratio is positively correlated with the degree of weathering and pedogenesis. The Rb/Sr value is highest in the S₀ (0.66), lower in the L₁ and L₀ (0.62 and 0.61), and lowest in the AS (0.58).

4.3.2. A-CN-K ternary diagram

The A-CN-K ternary diagram ($\text{Al}_2\text{O}_3\text{--CaO}^* + \text{Na}_2\text{O}\text{--K}_2\text{O}$), proposed by Nesbitt and Young (1982), quantitatively reveals the degree of feldspar weathering into secondary clay minerals relative to the parent rock. In the TKGC section, sample projection trends are parallel to and close to the A-CN line, but distant from the A-K line. This suggests that plagioclase feldspar underwent weathering and decomposition, with Ca and Na being leached out, leading to the formation of secondary aluminosilicate minerals (clay minerals), while K-feldspar remained mostly unaltered. The sample points from different stratigraphy are distributed at varying positions within the projection field. The S₀ samples are located in the upper part of the diagram, near the A apex, indicating a higher

degree of plagioclase weathering and transformation into secondary clay minerals. This suggests that the S₀ experienced more intense pedogenic modification. In contrast, the L samples plot lower and farther from the A apex, reflecting a lower degree of plagioclase decomposition

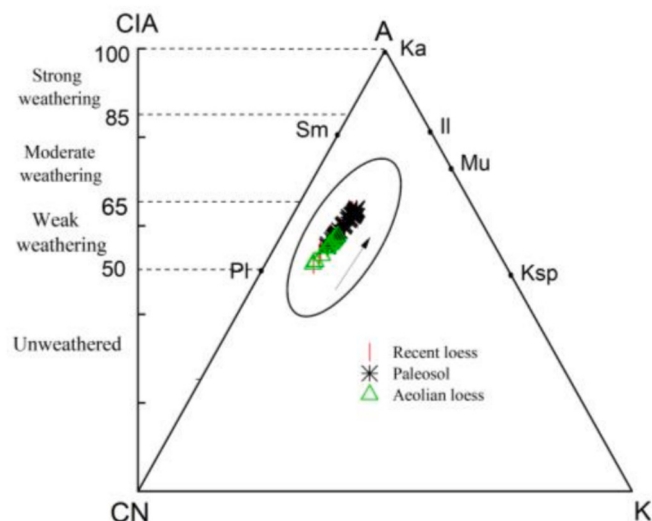


Fig. 7. A-CN-K ternary diagram of the TKGC section on the paleo-lakeshore terraces of the Zoige Basin.

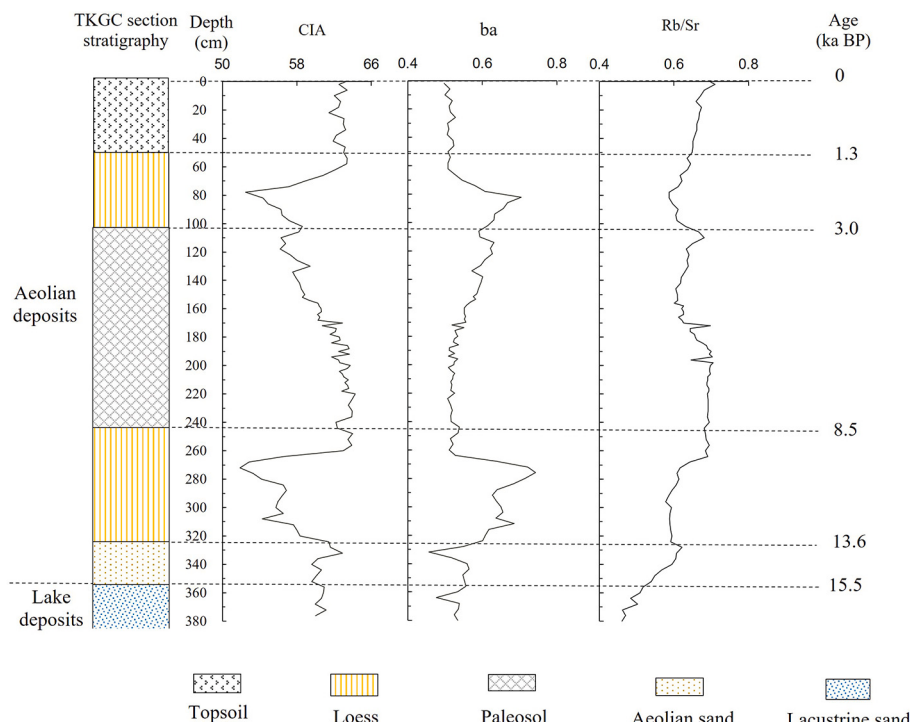


Fig. 6. Physicochemical parameter curves of the TKGC section on the paleo-lakeshore terraces of the Zoige Basin.

and weaker chemical weathering (Fig. 7).

4.3.3. Micromorphology

The micromorphological characteristics of the aeolian deposits above 354 cm in the TKGC section are characterized by angular to subangular grain edges. Primary minerals show signs of decomposition or the formation of secondary minerals. Voids are predominantly rounded or vesicular (Fig. 8f). The micromorphology of the lacustrine deposits below 354 cm differs significantly from the overlying aeolian deposits. There is an increased proportion of unstable minerals, and coarse grains have smooth edges without sharp angularities. The grain size is coarser than that of the aeolian deposits. Grain surfaces are intact and clean, with clear boundary outlines. The number of voids is relatively low, and their sizes are inconsistent (Fig. 8a-e). These micromorphological characteristics indicate that the sedimentary environment of the gray-green sand is distinctly different from that of the overlying aeolian deposits and closely resembles typical lacustrine sediments.

The micromorphological characteristics (mineral morphology, pedofeatures, and void characteristics) of different stratigraphy in the aeolian deposits exhibit clear distinctions, indicating divergent pedogenesis. Aeolian Sand (AS): The coarse grains are mostly angular, with

coarse grain sizes ranging from 100 to 600 μm . Mineral surfaces are clean, showing no obvious signs of weathering or alteration. Mineral grains are tightly packed, with very few voids. The humus content is low, primarily present as fine, rounded spots dispersed within the groundmass (Fig. 8e). Loess (L): The coarse grains have irregular edges, mostly angular, with grain sizes ranging from 100 to 500 μm . Plagioclase feldspar surfaces are clean with distinct angular boundaries. Mica surfaces are clean and unaltered, with occasional hornblende residues present. Plagioclase cleavage is clearly visible. The voids are sparse and relatively uniform, mostly sub-rounded in shape. The humus content is low and generally sub-rounded (Fig. 8c and d). Paleosol (S_0): The coarse grains exhibit smoother edges (sub-angular to sub-rounded). Plagioclase surfaces are cloudy and fissured, mica boundaries are blurred, and hornblende appears as residual spots, indicating significant weathering and mineral decomposition. Grain sizes are finer, generally between 10 and 200 μm . Numerous secondary calcite crystals are observed, either as needle-shaped or fibrous structures along void edges, or as coarser granular crystals, resulting from the leaching and accumulation of calcite. The void content is higher, and the void types are more diverse. Tubular and vesicular voids dominate, with a small number of planar and circular voids. The void shapes are complex, showing curves and extensions in multiple directions, or connecting with each other. A large

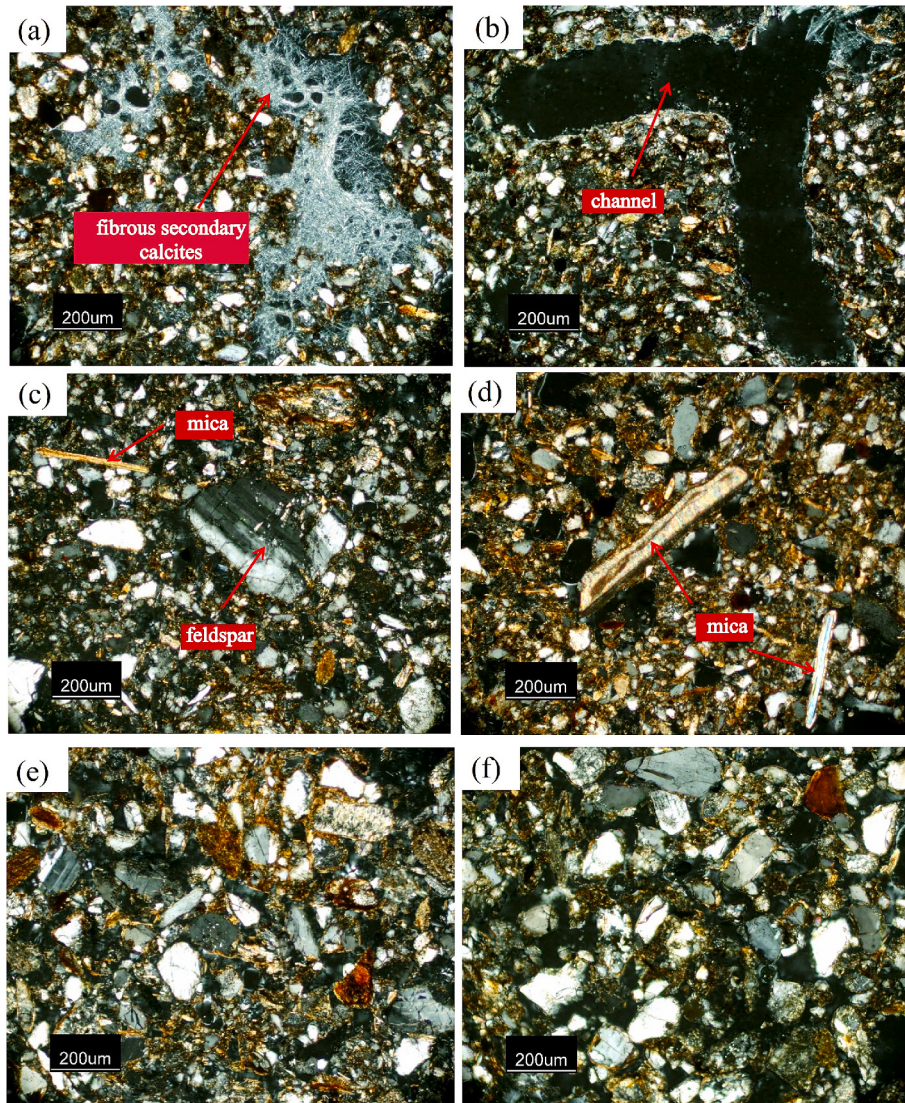


Fig. 8. Micromorphological features of the TKGC section on the paleo-lakeshore terraces of the Zoige Basin. (a) Paleosol (XPL 10 \times 10); (b) Paleosol (XPL 10 \times 10); (c) Recent loess (XPL 10 \times 10); (d) Aeolian loess 279 (XPL 10 \times 10); (e) Aeolian sand (XPL 10 \times 10); (f) Lacustrine sand (PPL 10 \times 10).

amount of humic colloids is present, appearing in strip, block, or round shapes (Fig. 8a and b).

5. Discussion

5.1. Chronostratigraphic framework and significance

The OSL dating results of the seven samples from the TKGC section show an increasing trend in age from bottom to top without any indication of age inversion, demonstrating the reliability of all OSL dates obtained. The Bacon age-depth model fitting for the TKGC section reveals a strong correlation between age and depth, enabling an accurate age framework for the stratigraphy (Fig. 9).

The TKGC section essentially represents a typical aeolian deposit sequence overlaying thick lacustrine sediments, with the stratigraphic boundary located at 354 cm, marking the transition between two distinct depositional environments. The basal age of the aeolian deposits directly indicates the earliest time when aeolian deposition began and has been preserved. The OSL date at the bottom of the aeolian deposits (at 345 cm depth) is 15.00 ± 0.49 ka. The Bacon age-depth model shows that the age at 354 cm (the boundary between lacustrine and aeolian facies) is 15.5 ka. This suggests that around 15.5 ka BP, the Tangke area transitioned from a lacustrine to a terrestrial environment, marking the onset of stable aeolian deposition which has been continuously preserved to the present day.

Since around 15.5 ka BP, stable aeolian deposition began; however, surface processes remained dynamic and underwent continuous changes. The properties and weathering intensity of the aeolian deposits varied synchronously, forming the stratigraphic sequence AS—L₁—S₀—L₀—TS. The basal age of the L₁ (at 300 cm depth) is 12.61 ± 0.45 ka. Based on the age-depth model, the stratigraphic boundary between the AS and the L₁ (at 324 cm depth) is dated to 13.6 ka,

suggesting that typical loess accumulation in this section commenced around 13.6 ka BP. The basal age of the S₀ (at 235 cm depth) is 8.31 ± 0.28 ka, and the model suggests the L₁—S₀ boundary (at 244 cm depth) is 8.5 ka. Comparable ages for the bottom of S₀ from other regional sections (OQC, CLQ, XQN) are 8.59 ± 0.39 ka, 8.25 ± 0.27 ka, and 8.44 ± 0.32 ka, respectively, further confirming that the development of the S₀ occurred around 8.5 ka BP (Wang et al., 2023; Zhao et al., 2024). The ages at the top (165 cm) and middle (120 cm) of the S₀ are 3.61 ± 0.12 ka and 4.48 ± 0.14 ka, respectively. The ages at the top (75 cm) and bottom (95 cm) of the L₀ are 1.80 ± 0.09 ka and 2.16 ± 0.11 ka, respectively. According to the age-depth model, the boundary between the S₀ and L₀ (104 cm) is dated to 3.0 ka. This suggests that the L₀ + TS was deposited during the late Holocene, beginning around 3.0 ka BP. Based on the above OSL age analyses, boundary ages between stratigraphy were established, and the final chronostratigraphic framework of the TKGC section is as follows: LS (>15.5 ka) — AS (15.5–13.6 ka) — L₁ (13.6–8.5 ka) — S₀ (8.5–3.0 ka) — L₀ (3.0–1.3 ka) — TS (1.3–0 ka).

5.2. Surface process changes since the late Pleistocene

Sedimentological and chronological analyses of the TKGC section reveal that the thick gray-green sandy layers formed at the paleo-lakeshore near Tangke represent littoral facies deposits, reflecting a lacustrine environment. With the disappearance of the Zoige paleolake, the paleo-lakeshore region transformed into a terrestrial environment. The thick lacustrine sand deposits became exposed at the surface, forming gently sloping terraces that provided favorable geomorphic conditions for the preservation of aeolian sediments. Exposed lakebeds and adjacent piedmont glacial outwash deposits supplied abundant sediment sources for regional aeolian activity. Around 15.5 ka BP, driven by changes in the surface environment, these paleo-lakeshore terraces underwent sustained accumulation of aeolian deposits and

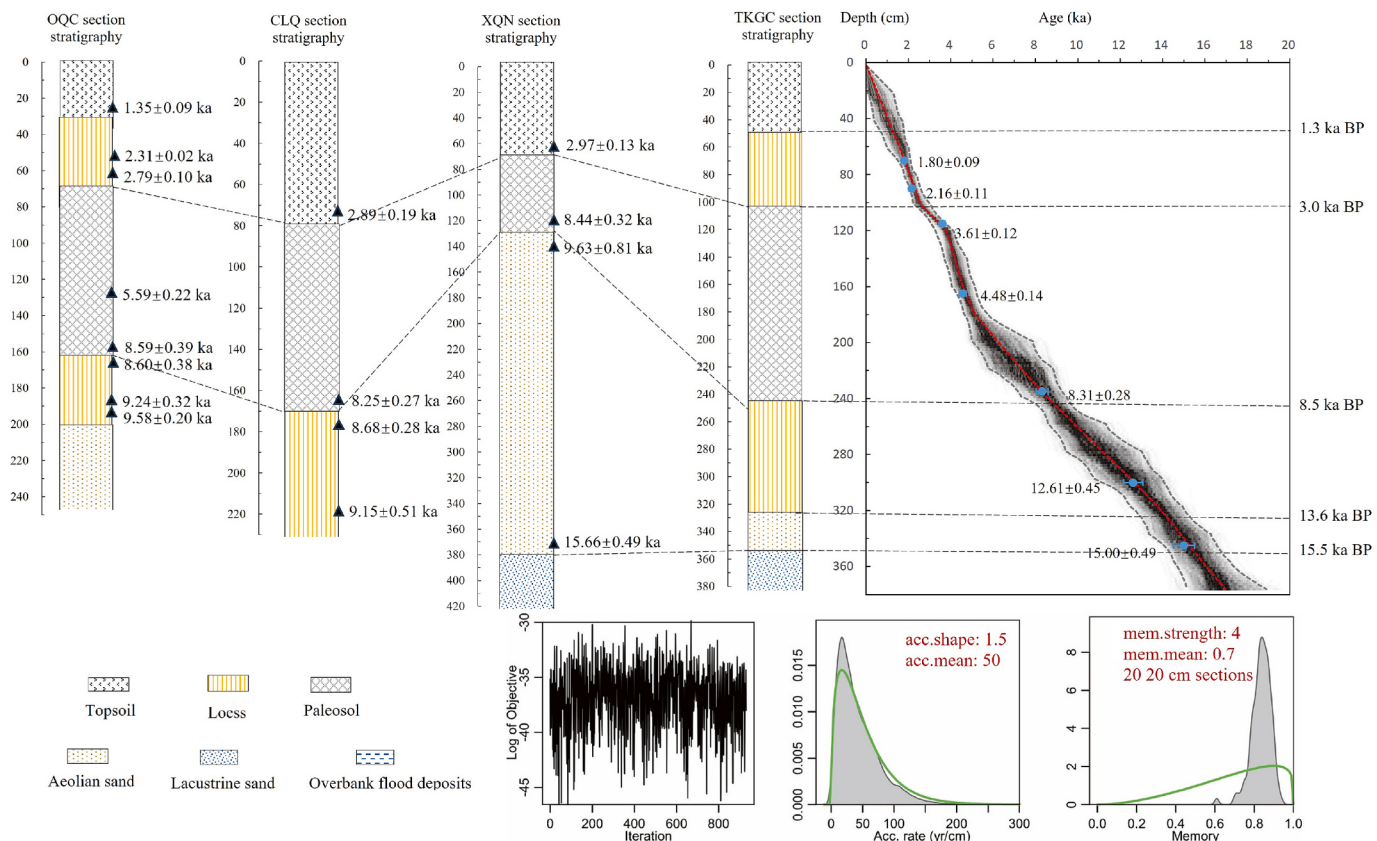


Fig. 9. Chronostratigraphic framework of the TKGC section on the paleo-lakeshore terraces of the Zoige Basin. OQC section (Zhao et al., 2024); CLQ and XQN section (Wang et al., 2023).

were well preserved, forming a loess–paleosol sequence that chronicles surface processes and environmental evolution since that time. The period since 15.5 ka BP can be divided into four stages:

15.5–13.6 ka BP, formation period of the aeolian sand (AS): The AS is dominated by sand-sized grains, with the lowest content of clay and fine silt. Md, Mz, and δ reach their highest values, indicating the coarsest and poorest sorted sediment. This reflects intense aeolian sand activity during the AS deposition period, leading to significant accumulation of dust. Micromorphological characteristics show predominantly angular grains with no obvious signs of mineral alteration; The humus is present as fine, rounded grains, and voids are small (Fig. 8e). This layer is characterized by elevated Na₂O, CaO contents and ba values, along with low magnetic susceptibility, Al₂O₃, MgO, K₂O contents, CIA, and Rb/Sr ratios. These indicators collectively suggest weak weathering and pedogenesis in the initial period after the disappearance of the lake, with minerals retaining their original depositional morphology and limited leaching of soluble elements. This implies cold and dry climate with strong wind activity, resulting in relatively coarse aeolian sands. Similar environmental evidence from the NE Tibetan Plateau supports this interpretation. The temperature reconstructed from U_K³⁷ for Qinghai Lake during this period was very low (Fig. 11g) (Hou et al., 2016), and the tree pollen from both Qinghai Lake and Dalinor lake also showed low values, indicating harsh climatic conditions dominated by aeolian dust deposition (Fig. 11c and f) (Cheng et al., 2013; Shen et al., 2005).

13.6–8.5 ka BP, development of aeolian loess (L₁): The L₁ is still dominated by sand-sized grains, though sand content decreases relative to AS. Higher Md, Mz, and δ values indicate relatively coarse grain sizes, suggesting that aeolian activity remained strong but was weaker than during the AS phase. The mineral grains exhibit well-defined angular boundaries and smooth crystal surfaces, with low humus content, a single void type, and small void diameters (Fig. 8d). High concentrations of Na₂O, CaO, and ba, along with low values of magnetic susceptibility, Al₂O₃, MgO, K₂O, CIA, and Rb/Sr, suggest weak post-depositional weathering and pedogenesis. The weak leaching of unstable elements

indicates a cold-dry climatic condition (Fig. 10a). Although aeolian deposition was still dominant around 13.6 ka BP, wind intensity declined significantly from the AS period, leading to typical loess accumulation. Other regional studies also support this dry-cold climate characterization during this period. In the Qinghai Lake area, vegetation was sparse, with both pollen and TOC content being low (Fig. 11b) (Shen et al., 2005). In the early Holocene, frequent aeolian sand activity characterized the NE Tibetan Plateau, with rapid sedimentation (Fig. 11d) (Chen et al., 2016). Around Dalinor Lake, the vegetation was desert steppe, and spruce and pine trees only grew in moist valleys, further indicating the dry and cold climatic conditions (Fig. 11c) (Cheng et al., 2013).

8.5–3.0 ka BP, paleosol (S₀) development: During this period, clay and fine silt contents increase while sand decreases. Md, Mz, and δ values decline, indicating weakened aeolian activity and predominance of pedogenesis. The micromorphological characteristics differ significantly from those of the underlying L₁. The proportion of unstable minerals declines, and minerals show distinct alteration features (fractured feldspar, altered hornblende and reduced mica). There is abundant humus colloid and faunal excrements in the soil (Fig. 8a and b). Low Na₂O, CaO, and ba values indicate strong leaching of soluble elements, while elevated magnetic susceptibility, Al₂O₃, MgO, K₂O, CIA, and Rb/Sr suggest enrichment of stable elements. These changes reflect intense pedogenesis altering mineral morphology and element distribution. The flourishing vegetation, active animal and microbial life indicate relatively warm and humid climate. These findings indicate that around 8.5 ka BP, the regional climate shifted from cold and arid to warm and humid, leading to a marked intensification of weathering and pedogenesis and resulting in the formation of the S₀ (Fig. 10b). Pollen reconstructions from the Zoige Basin show the highest precipitation between 8900 and 3200 BP (Fig. 11e) (Jin et al., 2018). During the mid-Holocene, extensive paleosol development occurred throughout the Qinghai Lake basin (Lu et al., 2015). The Dalinor Lake area was covered by dense spruce forests, with pollen concentrations reaching peak values (Fig. 11c) (Cheng et al., 2013). Aeolian sand activity decreased in the NE Tibetan Plateau, supporting the warm and humid climate of the mid-Holocene, consistent with the climatic conditions reconstructed in this study (Fig. 11d) (Chen et al., 2016).

3.0 ka BP to present, formation of recent loess and topsoil (L₀ + TS): Compared to S₀, the L₀ shows increased sand content and decreased clay and fine silt. Md, Mz, and δ values rise, indicating strengthened wind activity and more coarse grains. Unstable minerals increase relative to S₀, with coarser grains, clear angular boundaries, and low humus content. Void types are simple with fine void sizes (Fig. 8c). Leaching of Ca and Na is reduced, while Al, Mg, and K enrichment increases compared to S₀. These features reflect a climatic shift around 3.0 ka BP toward colder and drier conditions, with renewed aeolian activity and weakened pedogenesis, resulting in recent loess accumulation (Fig. 10c). Topsoil developed atop these recent loess deposits. During this period, the Qinghai Lake level underwent multiple fluctuations but exhibited an overall gradual decline. Aeolian activity in the Qinghai Lake basin began to intensify. And needle forests around Dalinor Lake decreased, replaced by grasslands (Liu et al., 2015; Lu et al., 2015; Cheng et al., 2013).

6. Conclusions

The disappearance of the Zoige paleolake led to the exposure of a large area of the former lakebed, giving rise to surface processes that differed from those of the preceding lacustrine phase. Various types of deposits with different origins subsequently formed, among which aeolian sediments serve as direct evidence for understanding regional aeolian activity and its changes. Multiple proxy indices analyses were conducted on the TKGC sites. The main findings and conclusions are as follows:

(1) The complete aeolian deposit sequence was deposited on the paleo-lakeshore terraces of the Tangke ancient city area. The

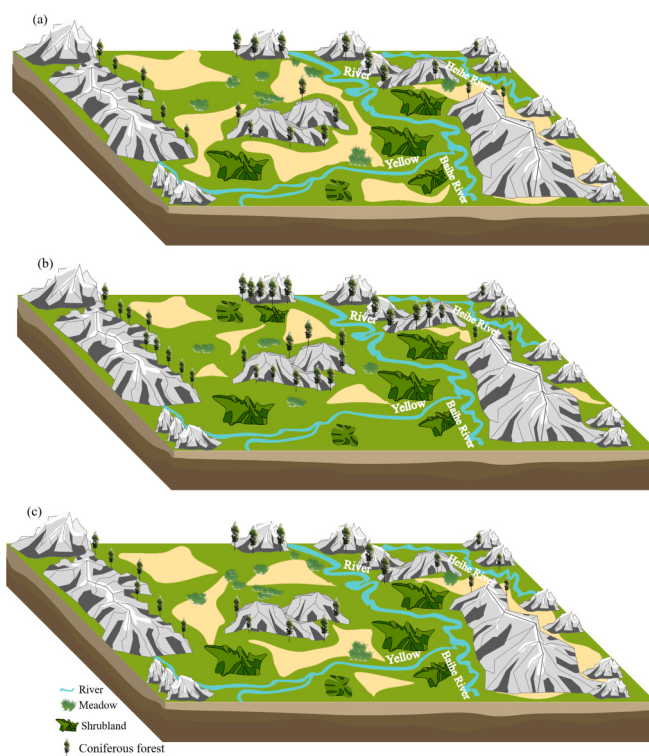


Fig. 10. (a) Early Holocene surface environmental changes around the TKGC; (b) Mid-Holocene surface environmental changes around the TKGC; (c) Late Holocene surface environmental changes around the TKGC.

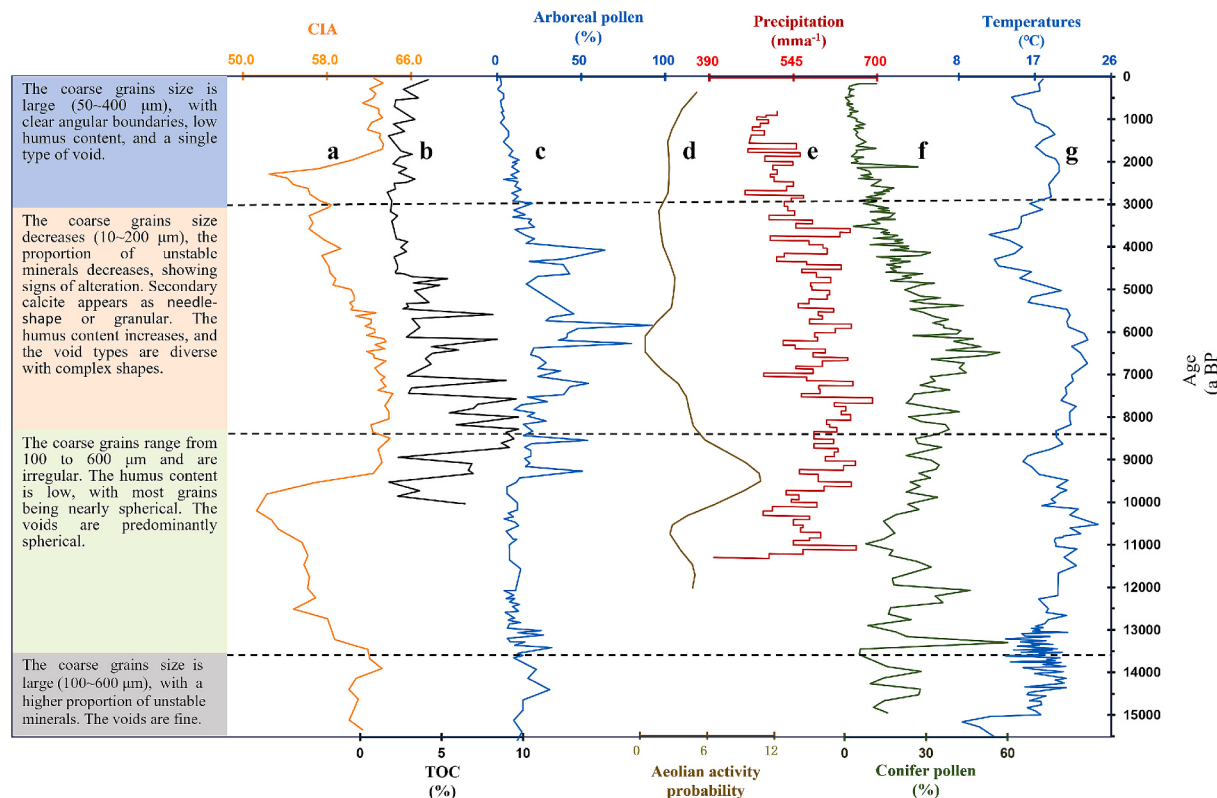


Fig. 11. (a) CIA content at the TKGC section; (b) TOC content in the Qinghai Lake (Shen et al., 2005); (c) The arboreal pollen percentage in the Dalinor Lake (Cheng et al., 2013); (d) Probability density for OSL ages of aeolian activity on the NE Tibetan Plateau (Chen et al., 2016); (e) Pollen-based annual precipitation reconstructed from the Zoige Basin (Jin et al., 2018); (f) The conifer pollen percentage of Qinghai Lake (Shen et al., 2005); (g) U^{37} inferred temperature record in the Qinghai Lake (Hou et al., 2016).

chronostratigraphic framework is as follows: aeolian sand (15.5–13.6 ka BP) — aeolian loess (13.6–8.5 ka BP) — paleosol (8.5–3.0 ka BP) — recent loess (3.0–1.3 ka BP) — topsoil (1.3–0 ka BP).

(2) Consistent with previous understandings of global climate change, the loess and paleosol sequences in the alpine Zoige basin reflect varying intensities of weathering and pedogenesis during different periods. Sedimentological, geochemical, and micromorphological evidence consistently indicate strong pedogenesis during the paleosol development, while pedogenic processes were weak during periods of aeolian sand and loess accumulation.

(3) By 15.5 ka BP, the paleo-lakeshore terrace in the Tangke ancient city area had transitioned into terrestrial landscape and began to accumulate stable aeolian deposits that have remained well preserved. These deposits provide valuable insights into surface processes and environmental changes that have occurred since 15.5 ka BP: Following the disappearance of the paleolake, from 15.5 to 13.6 ka BP, the region experienced harsh climatic conditions and intense aeolian activity, leading to the deposition of coarse-grained aeolian sand. Around 13.6 ka BP, aeolian activity declined, resulting in the accumulation of finer-grained aeolian loess. By 8.5 ka BP, the regional climate shifted from cold and arid to warm and humid, initiating the development of the paleosol. Around 3.0 ka BP, climatic conditions reverted to colder and drier states, enhancing aeolian processes and facilitating the formation of the recent loess layer. Subsequently, around 1.3 ka BP, the topsoil began to form atop the recent loess deposits.

CRediT authorship contribution statement

Dou Chen: Writing – original draft. **Jiangli Pang:** Resources, Project administration. **Xiaochun Zha:** Investigation. **Chunchang Huang:** Methodology. **Yuzhu Zhang:** Software, Resources. **Yali Zhou:** Software,

Methodology. **Yuqin Li:** Data curation. **Meihui Zhang:** Data curation. **Ruiqi Huang:** Data curation. **Xinran Fan:** Data curation.

Declaration of competing interest

The authors declare the following financial interests/personal relationships which may be considered as potential competing interests:

Jiangli Pang reports financial support, article publishing charges, equipment, drugs, or supplies, and travel were provided by National Natural Science Foundation of China. If there are other authors, they declare that they have no known competing financial interests or personal relationships that could have appeared to influence the work reported in this paper.

Data availability

The authors confirm that all data necessary for supporting the scientific findings of this paper have been provided.

Acknowledgements

This study was supported by the National Natural Science Foundation of China (42271046, 42277449, 41971116).

References

- Adamiec, G., Aitken, M.J., 1998. Dose-rate conversion factors: update. *Ancient TL* 16 (2), 37–50.
- Bai, J.H., Lu, Q.Q., Wang, J.J., Zhao, Q.Q., Ouyang, H., Deng, W., Li, A.N., 2013. Landscape pattern evolution processes of alpine wetlands and their driving factors in the Zoige Plateau of China. *J. Mt. Sci.* 10, 54–67.
- Chen, F.H., Wu, D., Chen, J.H., Zhou, A.F., Yu, J.Q., Shen, J., 2016. Holocene moisture and East Asian summer monsoon evolution in the northeastern Tibetan Plateau

- recorded by Lake Qinghai and its environs: a review of conflicting proxies. *Quat. Sci. Rev.* 154, 111–129.
- Chen, F.H., Zhang, J.F., Liu, J.B., Cao, X.Y., Hou, J.Z., Zhu, L.P., Xu, X.K., Liu, X.J., Wang, M.D., Wu, D., Huang, L.X., Zeng, T., Zhang, S., Huang, W., Zhang, X., Yang, K., 2020. Climate change, vegetation history, and landscape responses on the Tibetan Plateau during the Holocene: a comprehensive review. *Quat. Sci. Rev.* 243, 106444.
- Chen, D., Xiao, Q.L., Zhang, Y.Z., Wang, N.L., Wang, H.Y., Jia, Y.N., Zhu, Y., 2022. Weathering and pedogenesis of the Holocene aeolian loess-paleosol section and paleoclimate evolution in the Maqu reach in the Yellow River source area. *Geogr. Res.* 41 (8), 2277–2294.
- Cheng, B., Chen, F.H., Zhang, J.W., 2013. Palaeovegetational and palaeoenvironmental changes since the last deglacial in Gonghe Basin, northeast Tibetan Plateau. *J. Geogr. Sci.* 23 (1), 136–146.
- Dong, Z.B., Hu, G.Y., Yan, C.Z., Wang, W.L., Lu, J.F., 2010. Aeolian desertification and its causes in the Zoige Plateau of China's Qinghai-Tibetan Plateau. *Environ. Earth Sci.* 59, 1731–1740.
- Dong, Z.W., Brahnay, J., Kang, S.C., Elser, J., Wei, T., Jiao, X.Y., Shao, Y.P., 2020. Aeolian dust transport, cycle and influences in high-elevation cryosphere of the Tibetan Plateau region: New evidences from alpine snow and ice. *Earth Sci. Rev.* 211, 103408.
- Han, Y.X., Zha, X.C., Huang, C.C., Zhou, Y.L., Pang, J.L., Zhang, Y.Z., Wang, N., Bai, X., 2023. Sedimentary sequence and environment change of the first terrace in the outlet reach of the Yellow River in the Zoige Basin. *Sci. Geogr. Sin.* 43 (5), 922–931.
- Hou, J.Z., Huang, Y.S., Zhao, J.T., Liu, Z.H., Colman, S., An, Z.S., 2016. Large Holocene summer temperature oscillations and impact on the peopling of the northeastern Tibetan Plateau. *Geophys. Res. Lett.* 43 (3), 1323–1330.
- Hu, G.Y., Dong, Z.B., Lu, J.F., Yan, C.Z., 2015. The developmental trend and influencing factors of aeolian desertification in the Zoige Basin, eastern Qinghai-Tibet Plateau. *Aeolian Res.* 19, 275–281.
- Hu, G.Y., Yu, L.P., Dong, Z.B., Jin, H.J., Luo, D.L., Wang, Y.X., Lai, Z.P., 2017. Holocene aeolian activity in the Headwater Region of the Yellow River, Northeast Tibet Plateau, China: a first approach by using OSL-dating. *Catena* 149, 150–157.
- Hu, G.Y., Yu, L.P., Dong, Z.B., Lu, J.F., Li, J.Y., Wang, Y.X., Lai, Z.P., 2018. Holocene aeolian activity in the Zoige Basin, northeastern Tibetan Plateau, China. *Catena* 160, 321–328.
- Hu, G.Y., Hu, J.J., Yu, L.P., Yang, L.H., Liu, X.J., Xiao, F.J., Dong, Z.B., 2023. Holocene aeolian activity triggered by climate change and endorheic-exorheic drainage transition in the Headwater Region of the Yellow River. *Tibetan Plateau. Geomorphology* 441, 108890.
- Huang, C.C., 2021. Palaeoflood deposits in the Zoige Basin and the enlightenment on the formation of the Yellow River drainage system on the Tibetan Plateau. *Acta Geograph. Sin.* 76 (03), 612–625.
- Jia, Y.N., Zhang, Y.Z., Huang, C.C., Wang, N.L., Qiu, H.J., Wang, H.Y., Xiao, Q.L., Chen, D., Lin, X., Liu, C.H., Wang, C., Nan, Q., 2022a. Weathering and pedogenesis of the late Pleistocene and Holocene aeolian loess-paleosol sections in the Yellow River source area, NE Tibetan Plateau. *Palaeogeogr. Palaeoclimatol. Palaeoecol.* 600, 111065.
- Jia, Y.N., Zhang, Y.Z., Huang, C.C., Wang, N.L., Qiu, H.J., Wang, H.Y., Xiao, Q.L., Chen, D., Lin, X., Zhu, Y., Fu, L., Gu, K., Patton, N.R., 2022b. Late Pleistocene-Holocene aeolian loess-paleosol sections in the Yellow River source area on the northeast Tibetan Plateau: chronostratigraphy, sediment provenance, and implications for paleoclimate reconstruction. *Catena* 208, 10577.
- Jin, S.M., Wang, Y., Hou, G.L., Li, S.M., 2018. Quantitative reconstruction of precipitation on Qinghai-Tibet Plateau from Holocene pollen records. *Bull. Soil Water Conserv.* 38 (6), 169–176.
- Jin, Y., Zhang, Y.Z., Wang, N.L., Huang, C.C., Pang, J.L., Zhu, Y., Wang, L.S., Li, M.T., Wang, S.K., Cao, P.P., Xiao, Q.L., Zhou, J.P., Huang, X.L., Wang, Z.Y., 2025. Formation ages and environmental conditions of paleo-periglacial involutions in the Yellow River source area, northeastern Tibetan Plateau. *Palaeogeogr. Palaeoclimatol. Palaeoecol.* 659, 112659.
- Li, Z.W., Wang, Z.Y., Tian, S.M., Zhang, C.D., 2014. Variation of streamflow and sediment discharge rate and relationship with temperature change in Yellow River source area. *J. Sediment. Res.* 3, 28–35.
- Li, J., Sheng, Y., Wu, J.C., Feng, Z.L., Ning, Z.J., Hu, X.Y., Zhang, X.M., 2016. Mapping frozen soil distribution and modeling permafrost stability in the source area of the Yellow River. *Sci. Geogr. Sin.* 36 (4), 588–596.
- Li, J.C., Wang, Y., Zhang, L.S., Han, L.Y., Hu, G.Y., 2019. Aeolian desertification in China's northeastern Tibetan Plateau: Understanding the present through the past. *Catena* 172, 764–769.
- Li, D.B., Pan, B.Z., Zheng, X., Jiang, X.M., Zhao, G.N., Han, X., 2020. CDOM in the source regions of the Yangtze and Yellow Rivers, China: optical properties, possible sources, and their relationships with environmental variables. *Environ. Sci. Pol.* 27 (26), 32856–32873.
- Liu, X.J., Lai, Z.P., MADSEN, D., Zeng, F. M., 2015. Last deglacial and Holocene lake level variations of Qinghai Lake, North-Eastern Qinghai-Tibetan Plateau. *J. Quat. Sci.* 30 (3), 245–257.
- Lu, R.J., Jia, F.F., Gao, S.Y., Shang, Y., Li, J.F., Zhao, C., 2015. Holocene aeolian activity and climatic change in Qinghai Lake basin, northeastern Qinghai-Tibetan Plateau. *Palaeogeogr. Palaeoclimatol. Palaeoecol.* 430, 1–10.
- Murray, A.S., Wintle, A.G., 2000. Luminescence dating of quartz using an improved single-aliquot regenerative-dose protocol. *Radiat. Meas.* 32 (1), 57–73.
- Nesbitt, H.W., Young, G.M., 1982. Early Proterozoic climates and plate motions inferred from major element chemistry of lutites. *Nature* 299 (5885), 715–717.
- Nesbitt, H.W., Young, G.M., 1984. Prediction of some weathering trends of plutonic and volcanic rocks based on thermodynamic and kinetic considerations. *Geochim. Cosmochim. Acta* 48 (7), 1523–1534.
- Nesbitt, H.W., Young, G.M., 1989. Formation and diagenesis of weathering profiles. *J. Geol.* 97 (2), 129–147.
- Pang, J.L., Huang, C.C., Zhou, Y.L., Zha, X.C., Wang, X.Y., Zhao, X.K., Zhou, J.H., Li, Y.Q., Zhang, Y.Z., 2024. Soil development process depending on climate change in the first terrace of the Yellow River in Maqu valley since 3 ka. *Acta Geol. Sin.* 98 (7), 2269–2280.
- Prescott, J.R., Hutton, J.T., 1994. Cosmic ray contributions to dose rates for luminescence and ESR dating: large depths and long-term time variations. *Radiat. Meas.* 23, 497–500.
- Shen, J., Liu, X.Q., Ryo, M., Wang, S.M., Yang, X.D., 2005. A high-resolution climatic change since the late Glacial Age inferred from multi-proxy of sediments in Qinghai Lake. *Science. Sci. China (Ser. D: Earth Sci.)* 48 (6), 742–751.
- Stoops, G., 2003. Guidelines for Analysis and Description of Soil and Regolith Thin Sections. Madison, America.
- Wang, N., 2023. Age and Causes of the Yellow River Dissecting the Zoige Basin in the Eastern Tibetan Plateau. Shaanxi Normal University, Xian.
- Wang, J.Q., Wang, G.J., Liang, S.H., Du, H.B., Peng, H.M., 2021. Extraction and spatio-temporal analysis of vegetation coverage from 1996 to 2015 in the source region of the Yellow River. *Glaciol. and Geocryol.* 43 (2), 662–674.
- Wang, N., Zha, X.C., Huang, C.C., Zhang, Y.Z., Zhou, Y.L., Pang, J.L., Rong, X.Q., Shang, R.Q., Chai, J.N., 2023. Age and causes of the Yellow River dissecting the Zoige Basin in the eastern Tibetan Plateau. *China. Sci. Total Environ.* 857, 159481.
- Wang, X.Y., Pang, J.L., Huang, C.C., Zhou, Y.L., Zha, X.C., Li, Y.Q., Zhao, X.K., Zhai, Y., Sun, X.Q., 2024a. Chemical weathering degree of the late Holocene aeolian loess and climate change in Maqu Valley. *Sci. Geogr. Res.* 43 (7), 1911–1928.
- Wang, H.Y., Yang, J.H., Gao, F.Y., Wang, S.Y., Wang, Z.Q., Qu, W.X., Li, J.Y., Liu, X., Zhang, C.Y., Wang, L.K., Fan, Y.J., Yang, S.L., Xia, D.S., 2024b. Middle to late Holocene climate change in the monsoon-dominated southeastern Tibetan Plateau and its relationship with human activity. *Palaeogeogr. Palaeoclimatol. Palaeoecol.* 645, 112209.
- Yang, S.L., Liu, X.J., Cheng, T., Luo, Y.L., Li, Q., Liu, L., Chen, Z.X., 2021. Stepwise weakening of aeolian activities during the Holocene in the Gannan region Eastern Tibetan Plateau. *Front. Earth Sci.* 9, 686677.
- Yang, J.H., Wang, H.Y., Gao, F.Y., Wang, Z.Q., Wang, S.Y., Fan, Y.J., Li, T.Y., Liu, X., Qu, W.X., Li, J.Y., Zhang, Y.X., Chen, Z.X., Liu, L., Ayyamperumal, R., Yang, S.L., Xia, D.S., 2024. Holocene forcing of aeolian dust activity over the Tibetan Plateau and its surroundings. *Glob. Planet. Chang.* 235, 104400.
- You, Q.Y., Xue, X., Peng, F., Xu, M.H., Duan, H.C., Dong, S.Y., 2014. Comparison of ecosystem characteristics between degraded and intact alpine meadow in the Qinghai-Tibetan Plateau China. *Ecol. Eng.* 71, 133–143.
- Zhai, Y., Pang, J.L., Huang, C.C., Zhao, X.C., Zhou, Y.L., Li, Y.Q., Zhang, Y.Z., Sun, X.Q., Zhao, X.K., 2025. Particle endmembers characteristics of Amiola-South profile in the Zoige Basin and recorded climate change since 15 ka BP. *J. Desert Res.* 45 (2), 1–8.
- Zhao, X.K., Pang, J.L., Huang, C.C., Zhou, Y.L., Zha, X.C., Li, Y.Q., Zhang, Y.Z., Wang, X.Y., 2024. Chemical weathering characteristics and environmental significance of the aeolian loess-paleosol sequence on the second terrace of the Yellow River in the Maqu reach of Zoige Basin. *Acta Geograph. Sin.* 79 (05), 1177–1191.
- Zhi, Y., Liu, S.L., Wang, T., Duan, H.C., Kang, W.P., 2024. Quantifying the impact of natural and human activity factors on desertification in the Qinghai-Tibetan Plateau. *Catena* 246, 108392.
- Zhou, J.H., Zhou, Y.L., Huang, C.C., Zha, X.C., Pang, J.L., Zhang, Y.Z., Shang, R.Q., 2022. Chronology of the sedimentary sequence and the changes in surface processes along the Tangke reach of the Yellow River in the Zoige Basin. *Glaciol. and Geocryol.* 44, 1188–1202.
- Zhu, Y., Wang, S.K., Zhang, Y.Z., Wang, N.L., Huang, C.C., Pang, J.L., Jin, Y., Cao, P.P., Huang, X.L., Xiao, Q.L., Zhou, J.P., Li, M.T., 2025. Sedimentary stratigraphy of the second terrace of the Yellow River and its implications for the evolution of river-lake system within the Zoige Basin NE Tibetan Plateau. *Acta Geograph. Sin.* 80 (03), 758–777.